Turbulent Combustion Controls based on Local Flame Structure

Mamoru TANAHASHI, Satoshi KIKUTA, Nobuhiro SHIWAKU,
Shuji KATO, Shohei INOUE, Shohei TAKA and Toshio MIYAUCHI
Department of Mechanical and Aerospace Engineering, Tokyo Institute of Technology,
2-12-1 Ookayama, Meguro-ku, Tokyo 152-8552, Japan

In this paper, studies on turbulent combustion controls, which are supported by the 'Smart Control of Turbulence' project in last 5 years, have been summarized. To develop the theoretical strategy for controls of turbulent combustion, sound generation mechanism in turbulent reactive flows has been investigated from direct numerical simulation (DNS). It is suggested that the key point to develop control scheme of combustion noise is how to suppress the fluctuations of heat release rate and how to control the fine scale eddies which are related to turbulent energy dissipation rate and Reynolds stress terms. As the main sound source is the heat release rate, local flame structure has been investigated by DNS and advanced measurement techniques. DNS with detailed kinetic mechanism has been extended to three-dimensional field. Three-dimensional DNS of hydrogen-air turbulent premixed flames have been performed for different turbulence properties and different equivalence ratio by considering a detailed kinetic mechanism. The characteristics of local flame structure of turbulent premixed flames have been investigated by introducing proper representations of flame geometry and strain rate at the flame fronts. Three-dimensional DNS of methane-air turbulent premixed flames was also conducted by considering a reduced kinetic mechanism. The difference between hydrogen-air and methane-air turbulent premixed flames was discussed in details and possibilities of the local extinction of turbulent premixed flames were shown from the methane-air case. In addition to DNS, advanced measurement methods such as simultaneous CH-OH PLIF/PIV and a time-resolved PIV have been developed to investigate turbulent premixed flames. From the simultaneous CH-OH PLIF/PIV, Reynolds number and equivalence ratio effects on flame characteristics such as curvature of the flame fronts and strain rate on the flame surface were shown and the results were compared directly with DNS. In the development of the time-resolved stereoscopic PIV, it is shown that velocity measurement up to 26.7kHz is possible and the results represent dynamics of the turbulence structure very well. The time-resolved stereoscopic PIV can provides energy spectrums of three velocity components as well as the time-averaged feature of the turbulent flows with high accuracy. Based on the fundamental researches in the above, the turbulent combustion controls based on local flame structure were demonstrated on the swirl–stabilized combustor (0.2MW). The controls of the combustor were conduced by adding secondary fuel injection. The secondary fuel injectors are located at the center of the swirler. It has been demonstrated that combustion noise can be reduced about 10dB by adding continuous 1% secondary fuel injection and about 5dB more by controlling frequency of the secondary fuel injection. There is a most relevant frequency for the noise reduction. Furthermore, the lean limit has been extended to 0.2 without the increase of NOx production. The relation between local flame structure and pressure fluctuation in the combustor has been shown by the simultaneous measurement of CH-OH PLIF and pressure fluctuation in the combustor. The combustion-induced oscillations are well correlated with the beat frequency observed in the pressure fluctuation, and the global characteristics of the flame fronts are also correlated with the beat frequency. By adding this beat frequency to the secondary fuel injection, the maximum noise reduction can be achieved. The mechanism of the noise reduction by the secondary fuel injection was also clarified by simultaneous CH-OH PLIF/PIV. From these results, possibilities of active controls of turbulent combustion based on the local flame structure are presented.

1. Introduction

In the development of high efficiency combustor, it is important to reduce the combustion noise and to inhibit the combustion-driven oscillations with low NOx emission. It has been considered that most of combustion oscillations or combustion instabilities are caused by the feedback interaction between natural acoustic modes of combustor and oscillations of heat release rate (Rayleigh 1945). Since the combustion oscillations or instabilities may cause noise emission and break down of the combustor, a number of studies have been conducted to clarify the mechanism of the combustion instabilities and to develop the control strategies of combustion oscillation (Samaniego *et al.* 1993, Broda *et al.* 1998, Di Benedetto *et al.* 2002, Paschereit *et al.* 1999, Lieuwen *et al.* 2000, Gulati *et al.* 1992, Sivasegaram *et al.* 1995, Blonbou *et al.* 2000). From the viewpoint of pollution formation, NOx have a major impact on the environment and studies related to NOx reduction by passive or active controls have also been conducted (Poppe *et al.* 1998,

Delabroy *et al*. 1998, Murugappan *et al*. 2000). According to Rayleigh, one may easily control combustion oscillations by simply introducing an energy source out of phase with heat release rate. However, it has been demonstrated that successful control strategies depend on the combustion conditions or combustors (Gulati *et al.* 1992, Sivasegaram *et al.* 1995, Blonbou *et al.* 2000). Therefore, a detail understanding of the combustion oscillations and/or instability mechanism is necessary for an effective and robust active control of combustion. To obtain important factors for control of combustion oscillations, several experimental studies have been conducted for flame-acoustic interactions in unstable combustors using phase-locked measurements (Samaniego *et al.* 1993, Broda *et al.* 1998). Quantitative measurements of the flames response to acoustic perturbations have also been conducted (Poinsot *et al*. 1986, Harper *et al*. 2001). Recently, the effect of secondary fuel injection location on the effectiveness of active combustion control was studied in a laboratory-scale dump combustor at atmospheric pressure (Lee *et al*. 2000). Hong *et al*. (2002) has been conducted experiments to evaluate the control law under wide-range operation of a generic combustor using secondary fuel injection. Combustion control using secondary fuel injection has two advantages; one is that successful combustion control is possible using considerably small amount of energy and the second is that it reduces the actuator requirements. From these advantages, the secondary fuel injection method is desirable to suppress pressure fluctuations and to prevent lean blowout of the flame. On the other hand, optimum design has been required to minimize the amount of secondary fuel because it had been considered that secondary fuel injection might cause large amount of nitric oxide.

In this paper, sound generation mechanism in chemically reacting turbulent flows are briefly summarized in Sec. 2 to show our basic strategy for turbulent combustion controls based on local flame structure. As the fluctuation of the heat release rate is main sound source, investigations of the local flame structure by DNS are presented in Sec. 3. In Sec. 4, advanced experimental methods developed through this project are shown and local flame structure of turbulent premixed flames in the swirl-stabilized combustor are investigated by comparing the results of DNS. Controls of the swirl-stabilized combustor by secondary fuel injection are demonstrated in Sec. 5, where the mechanism of the noise reduction by the secondary fuel injection was also clarified by the advanced experimental methods.

2. Sound Generation Mechanism in Turbulent Reactive Flows

With the recent development of the computer technology, researches on the sound generation in the non-reacting flows become possible by DNS (Colonius *et al.* 1994, Lilley *et al.* 1994, Mitchell *et al.* 1995, Colonius *et al.* 1997). From the exact numerical results both in the near field and the far field, details of the acoustic source have been investigated and acoustic analogies such as Lighthill (1952) and Powell (1964) have been validated. However, almost all previous studies were restricted to two-dimensional and non-reacting cases due to the limitation of the computer resources. Therefore, the knowledge of the sound source and the acoustic analogies can not be applied directly to predictions of the sound in the turbulent combustion field.

In this study, sound generation mechanism has been investigated by direct numerical simulation (DNS) of compressible, chemically reacting flows (Li *et al.* 2000a, 2000b, 2001, Miyauchi *et al.* 2001, Choi *et al.* 2003). The effects of heat release on the mechanism of sound generation are investigated in fully developed turbulent state. The distributions of the Reynolds stress term and the entropy term are investigated by focusing on the heat release rate and the coherent fine scale eddy in turbulence.

As an acoustic analogy, Lighthill (1952) has rearranged the exact continuity and momentum equations into a wave equation as follow:

$$\frac{\partial^2 \rho'}{\partial t^2} - \frac{1}{M^2}\frac{\partial^2 \rho'}{\partial x_i \partial x_i} = \frac{\partial^2 T_{ij}}{\partial x_i \partial x_j}, \tag{1}$$

where T_{ij} is the Lighthill's turbulent stress tensor defined by

$$T_{ij} = \rho u_i u_j + \frac{1}{M^2}\delta_{ij}\left(\frac{1}{\gamma} p - \rho\right) - \frac{1}{\mathrm{Re}}\tau_{ij}. \tag{2}$$

In this study, the total acoustic source term (T) is decomposed into Reynolds stress term (T_R), entropy term (T_E), and viscous term (T_V) as follows:

$$T_R = \frac{\partial^2 (\rho u_i u_j)}{\partial x_i \partial x_j}, \quad T_E = \frac{\partial^2}{\partial x_i \partial x_j}\left[\frac{1}{M^2}\delta_{ij}\left(\frac{1}{\gamma} p - \rho\right)\right], \quad T_V = \frac{\partial^2}{\partial x_i \partial x_j}\left(-\frac{1}{\mathrm{Re}}\tau_{ij}\right), \tag{3}$$

$$T = T_R + T_E + T_V. \tag{4}$$

Figure 1 shows contour plots of the second invariant of the velocity gradient tensor and heat release rate in the fully developed turbulent state. The second invariant is defined by $Q=(W_{ij}W_{ij}-S_{ij}S_{ij})/2$, where S_{ij} and W_{ij} denote symmetric and asymmetric parts of the velocity gradient tensor, respectively. Our recent

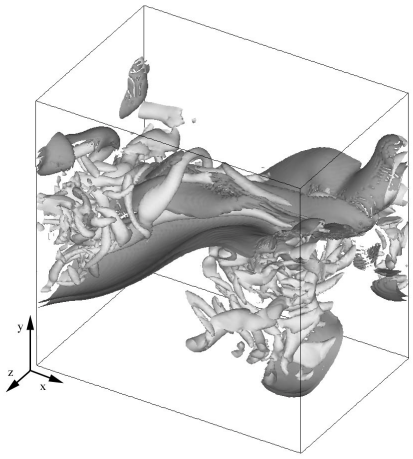

Fig. 1 Distributions of the second invariant (gray) and heat release rate (dark gray).

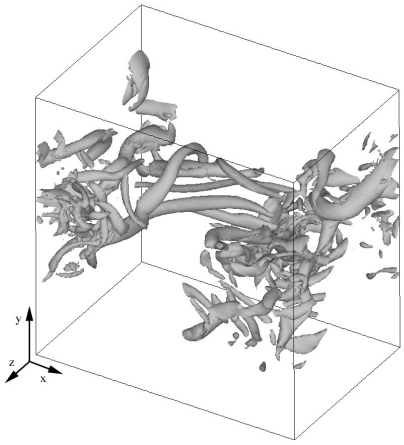

Fig. 2 Contour surfaces of Reynolds stress term of the acoustic source.

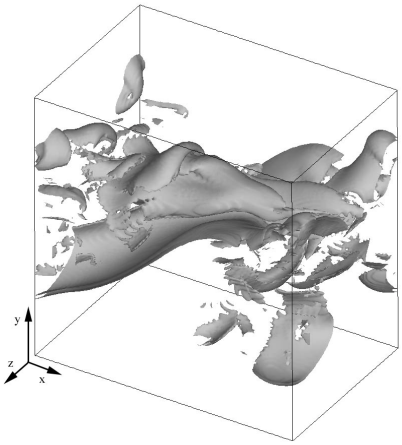

Fig. 3 Contour surfaces of entropy term of the acoustic source.

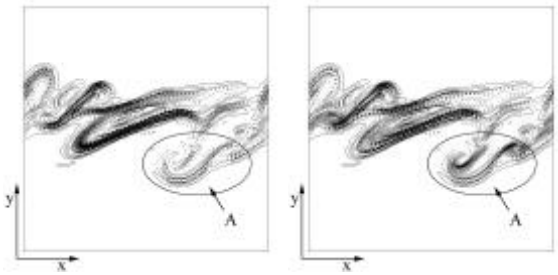

Fig. 4 Contour plots of the entropy term with heat release rate and energy dissipation rate in a typical cross section. (a): Gray: heat release rate Lines: T_E, (b): Gray: e; Lines: T_E.

studies on the fine scale structure of turbulence (Tanahashi *et al.* 2001, 2004a) have shown that turbulence is composed of a universal fine scale structure: coherent fine scale eddies, and these coherent fine scale eddies of turbulence are well represented by the positive Q region in turbulence. Figure 2 shows the contour surfaces of Reynolds stress term of the acoustic source. With the transition to turbulence, lots of tube-like structures are observed similar to the second invariant in Fig. 1. This is because that the Reynolds stress term can be exactly expressed by the second invariant as T_R=-2Q in the limit of the incompressible flow. Figure 2 suggests that the relation between these two variables sustained even in the chemically reacting turbulence. Therefore, the coherent fine scale eddy plays important roles in the sound generation not only in non-reacting turbulence but also in reacting turbulence.

Figure 3 shows the contour surfaces of the entropy term. In the non-reacting turbulent flows, the entropy term shows sheet-like structure around coherent fine scale eddies in the fully-developed state. However, in the reacting turbulent flows, the entropy term shows significantly large values. Compared with the contour surfaces of heat release rate in Fig. 1, it can be seen that the distribution of entropy term is consistent with that of the heat release rate. To show details of the entropy term, contour plots of the entropy term are superimposed on the distributions of the heat release rate and the turbulent energy dissipation rate on a typical cross section in Fig. 4. The turbulent energy dissipation rate (e) is defined by $e = 2nS'_{ij}S'_{ij}$, where S'_{ij} represents strain rate tensor of velocity fluctuations. From these figures, it is clearly shown that the distribution of entropy term is mainly determined by the heat release rate. The entropy term shows negative values in the regions with high heat release rate and shows positive values around these regions. However, in core region denoted by a circle, the entropy term shows relatively large values despite low heat release rate. In these regions, the entropy term coincides with the distribution of the energy dissipation rate. Note that the distribution of entropy term is determined by the energy dissipation rate in the non-reacting turbulence. These results suggest that the entropy term is mainly determined by the heat release rate, while it is influenced by the energy dissipation rate in low heat release rate regions.

Table 1 Numerical parameters of DNS of hydrogen/air turbulent premixed flames. d_L: laminar flame thickness defined by $d_L=(T_b-T_u)/(\partial T/\partial x)_{max}$ where T_u and T_b denote temperature in the unburned and burned side, D: the most expected diameter of the coherent fine scale eddy, $Re_l=lu'_{rms}/\nu$, $Re_l=lu'_{rms}/\nu$, L_i: length of the computational domain in the i direction (mm), N_i: grid points in the i direction.

ID	u'_{rms}/S_L	l/d_F	l/d_L	D/d_L	Re_l	Re_l	$L_x \times L_y \times L_z$	$N_x \times N_y \times N_z$
R37LL	0.85	169	3.38	0.78	143.6	37.4	5.0×10.0×10.0	257×256×256
R37MM	1.70	84.3	1.69	0.39	143.6	37.4	10.0×5.0×5.0	513×128×128
R37HS	3.41	42.2	0.85	0.19	143.6	37.4	5.0×2.5×2.5	513×128×128
R60HM	3.39	90.1	1.81	0.28	203.0	60.8	5.0×5.0×5.0	513×192×192
R97HM	5.78	122	2.45	0.19	515.0	97.1	7.4×7.4×7.4	1115×384×384

The far field pressure fluctuation was also predicted using acoustic analogies. By comparing the predicted far field sound with DNS result, Lighthill's and Powell's acoustic analogies are evaluated. For turbulent flames, the far field sound seems to be predicted only by considering the entropy term, while the Reynolds term should be included to predict the sound radiated in the process of the transition to turbulence. These results suggest that the key point to develop control scheme of combustion noise is how to suppress the fluctuations of heat release rate and how to control the fine scale eddies which are related to turbulent energy dissipation rate and Reynolds stress terms.

3. Investigation of Local Flame Structure by DNS

To develop the active control scheme of the combustors, the understandings of the flame structures in the combustor are necessary because the main sound source is fluctuation of the heat release rate. Especially, detailed information about heat release rate or pressure fluctuations in the turbulent flames is quite important for development of active control scheme. The characteristics of the turbulent premixed flames have been classified by the ratio of the laminar burning velocity (S_L) to the turbulence intensity (u'_{rms}) and the ratio of the laminar flame thickness (d_F) to the turbulence length scale (l) (Borghi 1985, Peters 1986, 1992). Peters (1992) has proposed the combustion diagram based on the relation between u'_{rms}/S_L and l/d_F, and classified the flame structure into four regimes; wrinkled flamelets, corrugated flamelets, thin reaction zones and broken reaction zones. In the wrinkled flamelets and the corrugated flamelets regimes, flame structure is considered to be approximated by the laminar flamelets with small curvature under strain field, whereas characteristics of the flame elements in the thin reaction zones and the broken reaction zones are supposed to be quite different from that of laminar flame.

From three-dimensional direct numerical simulations (DNS) of turbulent premixed flames, actual local flame structure in turbulence were investigated (Tanahashi *et al.* 2000a, 2002, Bell *et al.* 2002, Jenkins and Cant 2002, Sreedhara and Lakshmisha 2002). In the corrugated flamelets regime, local flame structure has been related with the curvature of the flame front and strain rate tangential to the flame front because the flame displacement may correlate with these two factors (Poinsot *et al.* 1990, Baum *et al.* 1994, Chen *et al.* 1998). Since the curvature and the tangential strain rate could be defined easily in two-dimensional field, mean curvature and total strain rate are used to classified the local flame elements even in the three-dimensional field as an extension of the analysis of two-dimensional DNS of turbulent premixed flames (Baum *et al.* 1994, Chen *et al.* 1998, Tanahashi *et al.* 1998, Saito *et al.* 2002). Tanahashi *et al.* (2000a) have shown that the flame/vortex interaction in fine scales are classified into the three type; (i) the fine scale eddies perpendicular to the flame enhance the heat release rate by their strong axial flow, (ii) the eddies parallel to the flame front enhance the heat release rate by the convection of the unburned mixture due to the strong swirling motion and (iii) the eddies perpendicular to the flame suppress the heat release rate. Since these flame/vortex interactions show strong three-dimensional feature, proper representation of the flame shape and strain rate at the flame are required. Jenkins and Cant (2002) have calculated two principal curvatures to investigate the effects of the three-dimensionality of the flame surface. Especially, three-dimensional flame structure such as the handgrip and spire structures (Nada *et al.* 2004) can not be represented by the mean curvature.

It is well known that responses of flame structure to flow field such as strain rate are different for fuels. To investigate turbulent flame structure in details, three-dimensional DNS of hydrocarbon fuels are required. For hydrocarbons, several tens species and several hundreds elementary reactions have to be included in DNS. DNS of turbulent combustion have been extended to hydrocarbon fuels such as methane and propane from simple hydrogen fuel (Echekki and Chen 1996, Chen *et al.* 1998, Saito *et al.* 2002). However, almost all previous studies were restricted to two-dimensional calculations due to the limitation of computer resources. To realize three-dimensional DNS, high accurate reduced kinetic mechanism which are available for turbulent combustion should be developed.

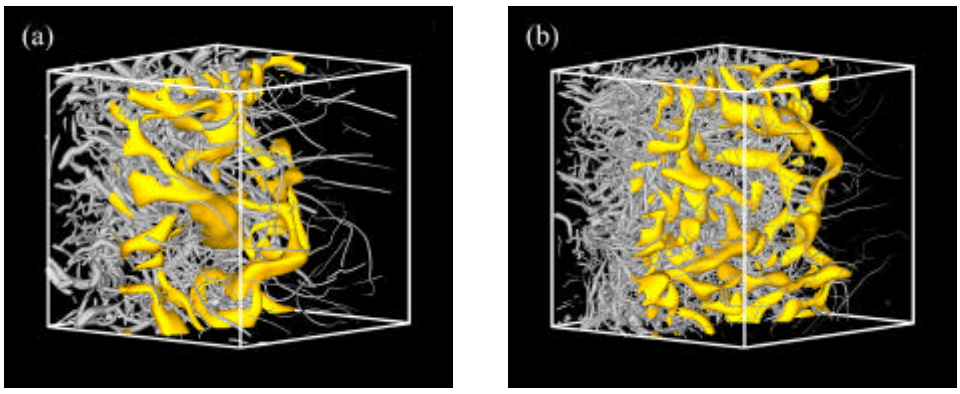

Fig. 5 Contour surfaces of the heat release rate ($DH>DH_L$) with the axes of the fine scale eddies for R37MM(a) and R60HM(b).

In this study, three dimensional DNS of hydrogen-air turbulent premixed flames is conducted up to Re_l=97.1 (Re_l=515.0) to investigate the importance of three-dimensional structures in turbulent premixed flames by using proper flame surface representation and strain rate decomposition. Effects of equivalence ratio on the local flame structure are also investigated by using DNS results of hydrogen-air turbulent premixed flames. Furthermore, three-dimensional DNS of methane-air turbulent premixed flames are conducted with a reduced kinetic mechanism to investigate fuel effects on the local flame structures and local extinction mechanism of premixed flames in high intensity turbulence.

3.1 Three-Dimensional DNS of Hydrogen-Air Turbulent Premixed Flames

In this study, DNSs of hydrogen/air turbulent premixed flames with Re_l=60.8 and 97.1 are conducted with a detailed kinetic mechanism and realistic thermal and transport properties in addition to previous DNSs for Re_l=37.4 (Tanahashi *et al.* 2000a, 2002). The detailed kinetic mechanism that is used in this study consists of 12 species and 27 elementary reactions (Gutheil *et al.* 1993). Detailed description about the DNS code can be found in our previous papers (Tanahashi *et al.* 2000a, 2002). Numerical parameters of DNSs are listed in Table 1. R37LL, R37MM and R37HS correspond to the DNSs reported by Tanahashi *et al.* (2000a, 2002) for Re_l=37.4. R60HM is conducted for Re_l=60.8 with conditions of u'_{rms}/S_L=3.39 and l/d_F=90.1 and R97HM is conducted for Re_l=97.1 with conditions of u'_{rms}/S_L =5.78 and l/d_F =122. All of DNS were conducted for f=1.0, 700K and 0.1MPa. R37LL is classified in the wrinkled flamelets, R37MM and R60HM are in the corrugated flamelets, R37HS and R97HM are located near the boundary of the corrugated flamelets and the thin reaction zones. In this sturdy, R37MM and R60HM are analyzed to investigate the three-dimensional flame structure in the corrugated flamelets regime.

3.1.1 Flame Geometry and Heat Release Rate

Figure 5 shows contour surfaces of heat release rate and axis distributions of the fine scale eddies for R37MM and R60HM. The contour level of the heat release rate is $DH/DH_L > 1.0$, where DH_L denotes the maximum heat release rate of the laminar flame. The thickness of the axis is drawn to be proportional to the square root of the second invariant of the velocity gradient tensor on the axis. The second invariant is normalized by u'_{rms} and Kolmogorov micro scale (h) in the unburned side. Thicker eddy possesses stronger swirling motion around the eddy. Note that the most expected diameter of these fine scale eddies is 8h and the maximum azimuthal velocity reaches to 3 - 4u'_{rms} (Tanahashi *et al.* 2001). As shown by our previous study (Tanahashi *et al.* 2000a), fine scale eddies in the unburned turbulence have great contribution to wrinkling of the flame surface and enhancement of the heat release rate. The fine scale eddies in the unburned mixture are weakened behind the flame front by the viscosity increase and the expansion of fluid, while strong eddies can survive in the burned side. For high Reynolds number case (R60HM), the number density of the fine scale eddies in the unit volume of the integral length scale (l^3) increases with the increase of Re_l (Tanahashi *et al.* 2000b). The wrinkling of the flame surfaces also increases for higher Reynolds number case. The spatial scale of the fluctuation of the heat release rate becomes small for high Reynolds number case.

Figure 6 shows probability density functions (pdf) of the local heat release rate. In this study, flame fronts are defined as points at which temperature gradient shows a local maximum value and the local heat release rate denotes maximum heat release rate in a flame element. With the increase of turbulent intensity or the decrease of turbulence length scale for the same Reynolds number, the maximum heat release rate increases and reaches to 1.3DH_L as shown by the previous study (Tanahashi *et al.* 2002). For the high Reynolds number case, probabilities for high local heat release rate increase compared with low

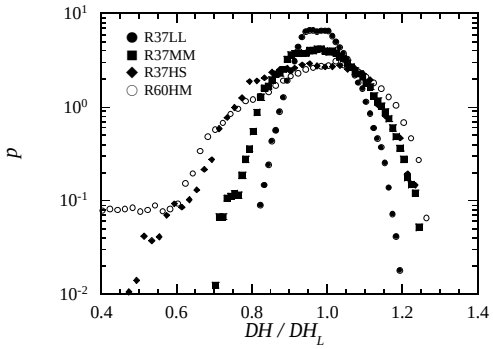

Fig. 6 Probability density functions of the local heat release rate.

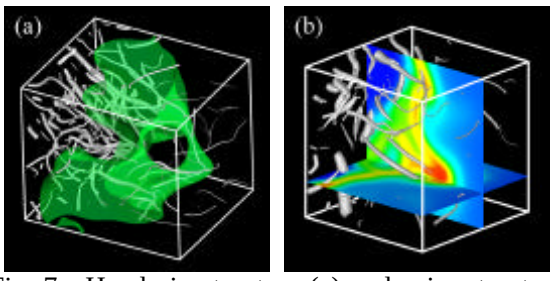

Fig. 7 Handgrip structure (a) and spire structure (b). Contour surface of temperature (1400K) and axes distribution of fine scale eddy are shown in (a), distribution of heat release rate on typical plane are presented with axes of the fine scale eddies in (b).

Reynolds number cases. Although elements with low heat release rate increase for high Reynolds number case, the probabilities of those are comparable to R37HS of which u'_{rms}/S_L is close to the high Reynolds number case.

Since the turbulent flames in these conditions can be classified in the corrugated flamelets regime, the flame surface is connected three-dimensionally. However, fluctuation of the heat release rate is relatively high along the flame surfaces and three-dimensional flame structure can be observed. Figure 7 shows the handgrip and spire structure which have been reported by our previous study (Nada *et al.* 2004). The handgrip structure is created by the intrusion of the strong fine scale eddies near the flame front. The created handgrip-like unburned mixture is heated by the surrounding burned gas and burn out quickly with heat release rate higher than $1.2DH_L$. The spire structure is also created by interaction between flame and the fine scale eddies perpendicular to the flame front. At cusp of the spire structure, heat release rate reaches $1.2DH_L$ even in the wrinkled flamelets regime (Nada *et al.* 2004). These flame structures are hardly approximated by laminar flamelets even though turbulent flames are classified in the corrugated flamelets regime. Although these structures enhance local heat release rate, contribution to the total burning velocity is relatively low for low Reynolds number cases such as R37LL and R37MM. For high Reynolds number flows, however, appearance of these three-dimensional structure increases because of high probability of the fine scale eddies which possess azimuthal velocity faster than S_L.

3.1.2 Flame Shape Classification

In most of previous studies, mean curvature has been used to represent flame surface geometry. In general, mean curvature is defined by $k=k_1+k_2$, where k_1 and k_2 represent principal curvatures of the flame front. Figure 8 shows pdfs of the mean curvature of the flame front. The curvature is defined to be positive value for the flame element convex toward the burned side and is non-dimensionalized by d_L in Fig. 8(a) and by h in Fig. 8(b). The maximum curvature for high Reynolds number case is larger than those for low Reynolds number cases and is $k = 30/d_L$. However, if k is non-dimensionalized by h, k is ranging in $|k| < 1/h$, which consists with our previous results for low Reynolds number cases (Tanahashi *et al.* 2000a, Nada *et al.* 2004). It has been shown that the local heat release rate is well correlated with the mean curvature and the flame element convex toward unburned side tends to show high heat release rate (Tanahashi *et al.* 2000a, 2002, Nada *et al.* 2004). However, three-dimensional structures such as the handgrip and spire structures are hardly represented by the mean curvature. Therefore, two principal curvatures are calculated from DNS results. Figure 9 shows joint pdfs of k_1 and k_2. Note that probability difference between neighboring contour lines is 2.0. From the two principal curvatures, flame shape can be classified into spherical surface convex toward the burned side (S-B), cylindrical surface convex toward the burned side (C-B), hyperboloidal surface (HB), cylindrical surface convex toward the unburned side (C-U) and spherical surface convex toward the unburned side (S-U). In Fig. 9, typical flame shapes are shown schematically, where the arrow denotes the burned side. Figure 9 shows that the principal curvatures are also normalized by $1/h$ and their maximum value is $1/h$. In Table 2, fraction of flame elements in each flame shape are shown for R37MM and R60HM. For low Reynolds number case, number of flame elements in C-U and S-U regimes is larger than that in C-B and S-B regimes. However, for high Reynolds number case, there are large number of flame elements in C-B and S-B regimes. Flame elements in S-B attribute to the spire and handgrip structures, and those in C-B regime are mainly created by fine scale eddies parallel to the flame front.

Mean local heat release rate conditioned with the principal curvatures are shown in Fig. 10 by colors with contour lines of joint pdf of k_1 and k_2. The heat release rate is normalized by DH_L. The mean heat release rate is well correlated with the flame shape and the flame elements in C-B and S-B show high heat

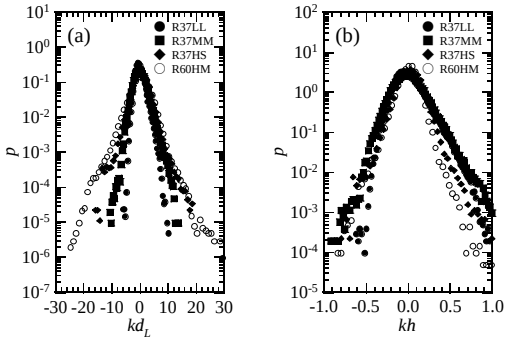

Fig. 8 Probability density functions of the mean curvature of flame front normalized by laminar flame thickness(a) and Kolmogorov micro scale in the unburned side(b).

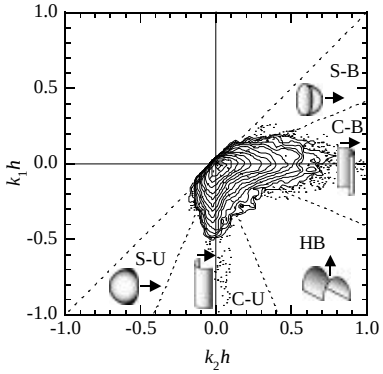

Fig. 9 Joint probability density functions of the principal curvatures for R37MM.

Table 2 Classification of flame element shape and contribution of flame element shape to the total heat release rate (values in parentheses).

	S-B [%]	C-B [%]	HB [%]	C-U [%]	S-U [%]
R37MM	2.38 (2.65)	33.55 (36.58)	21.13 (22.24)	36.25 (33.44)	5.68 (5.08)
R60HM	4.07 (4.62)	41.08 (45.08)	23.96 (23.48)	28.13 (24.57)	2.76 (2.25)

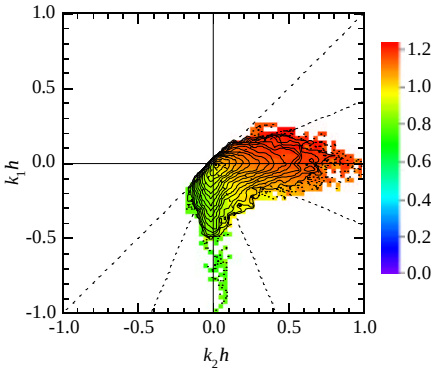

Fig. 10 Mean local heat release rate conditioned with the principal curvatures for R37MM.

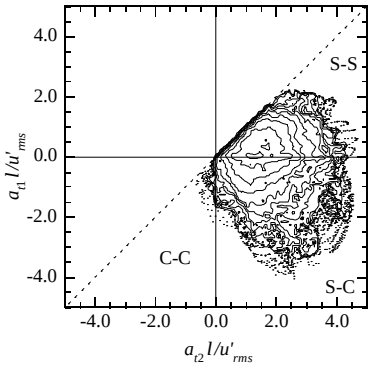

Fig. 11 Joint probability density functions of the tangential strain rates of flame front for R37MM.

release rate. This tendency is excessively emphasized for the high Reynolds number case. In Table 2, contributions of each flame element shape for the total heat release rate is included. For high Reynolds number case, contributions of C-B and S-B regimes are clearly high and make up about 50% of the total heat release rate. These results suggest that C-B and S-B flame elements would dominate the total heat release rate and the turbulent burning velocity in high Reynolds number turbulent premixed flames.

3.1.3 Strain Rate Classification on the Flame Surface

The strain rate tangential to the flame front has been discussed by $a_t=\boldsymbol{t}_1\boldsymbol{t}_1:\nabla\boldsymbol{u}+\boldsymbol{t}_2\boldsymbol{t}_2:\nabla\boldsymbol{u}$, where $\boldsymbol{t}_1$ and $\boldsymbol{t}_2$ represent unit vectors tangential to the flame front and are satisfying a relation of $\boldsymbol{t}_1\cdot\boldsymbol{t}_2=0$ (Candel and Poinsot 1990). In this study, we introduce the minimum and the maximum strain rate on the flame surface to investigate strain rate effect correctly. Figure 11 shows joint pdfs of the minimum and maximum strain rate. The minimum and maximum strain rates are denoted by a_{t1} and a_{t2}. As the mean strain rate is scaled by u'_{rms}/l (Tanahashi *et al.* 2000a, 2002), a_{t1} and a_{t2} are normalized by u'_{rms}/l. From a_{t1} and a_{t2}, the tangential strain rate on the flame surface can be classified into three types; stretching in the two directions (S-S), stretching and compression in each direction (S-C), and compression in two direction (C-C). The most expected strain field is simple two-dimensional strain rate of the order of u'_{rms}/l (a_{t1}=0 and a_{t2}= u'_{rms}/l). In Table 3, flame elements are classified by the tangential strain rates. For low Reynolds number cases, the flame elements in S-S regime is more than 50% and almost all of flame elements are under the stretching in one direction at least. Flame elements in C-C regime are scarcely observed. For high Reynolds number case, number of flame element in S-C regime increases and exceeds 50%. It should be noted that flame elements in S-S regime could be approximated by laminar flames observed in counter-flow flame, whereas it is not the case for those in S-C regime. Mean local heat release rate conditioned with tangential strain rates are shown by colors in Fig. 12. The contour lines in Fig. 12

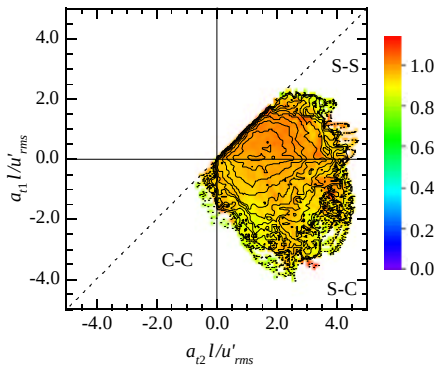

Fig. 12 Mean local heat release rate conditioned with the tangential strain rates for R37MM(a).

Table 3 Classification of flame elements due to tangential strain rates.

	S-S [%]	S-C [%]	C-C [%]
R37MM	56.61	43.26	0.129
R60HM	43.89	55.76	0.351

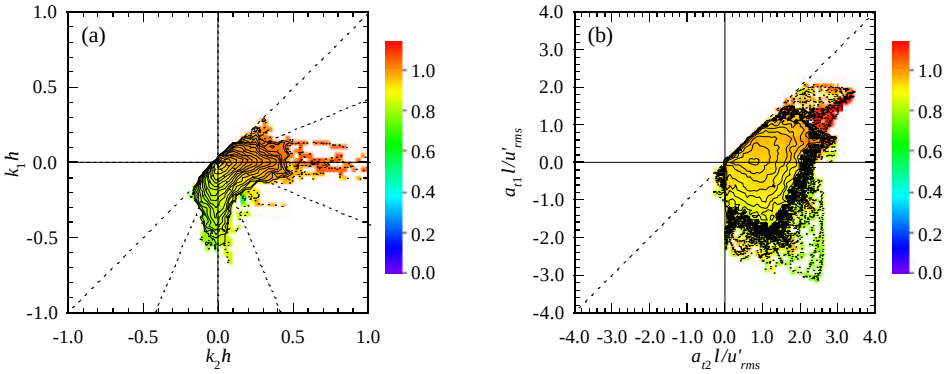

Fig. 13 Mean local heat release rate conditioned with the principal curvatures (a) and mean local heat release rate conditioned with the tangential strain rates (b) for f=0.6.

represent joint pdf of a_{t1} and a_{t2}. Flame elements in S-S regime tend to show high heat release rate for low Reynolds number case, but no correlation between strain rates and the heat release rate can be observed for high Reynolds number case. Table 3 includes contribution of the strain rate on the total heat release rate. As for the heat release rate, no systematic relation with tangential strain rate can be observed.

3.1.4 Effects of Equivalent Ratio

Figure 13 shows the probability density functions of the principal curvatures and tangential strain rates for low equivalent ratio case (f=0.6). Similar to the previous figures, mean heat release rate conditioned with the curvatures and strain rate are presented by color distributions. Compared with f=1.0 cases in Fig. 10, correlation between local heat release rate and the curvatures becomes weaker for f=0.6. However, the local heat release rate correlate with the tangential strain rate for f=0.6. Flame elements under the stretching into two tangential directions tend to show high heat release rate. These results suggest that local flame structure in lean conditions is dominated by the strain field due to turbulent motions in the unburned side.

3.2 Three-Dimensional DNS of Methane-Air Turbulent Premixed Flames

In this study, three-dimensional DNS of methane-air turbulent premixed flames are conducted with a reduced kinetic mechanism to investigate fuel effects on the local flame structures and local extinction mechanism of premixed flames in high intensity turbulence (Tanahashi *et al.* 2004d). First, two-dimensional DNS with two-different detailed kinetic mechanism and a reduced kinetic mechanism were conducted to validate performance of a reduced kinetic mechanism for DNS of turbulent combustion. The validated reduced kinetic mechanism is applied for three-dimensional DNS and the results are analyzed to investigate fuel effects on the local flame structures and local extinction mechanism of turbulent premixed flames. Numerical methods are similar to our previous DNS of hydrogen-air turbulent premixed flames (Tanahashi *et al.* 2000a, 2002, Nada *et al.* 2004). For two-dimensional DNS, two detailed kinetic mechanisms; GRI-Mech. 2.11 (49 reactive species and 279 elementary reactions) and Miller and Bowman (Miller and Bowman 1989) (51 reactive species and 235 elementary reactions), and a reduced kinetic mechanism (MeCH-19) based on GRI-Mech. 2.11, which includes 23 reactive species and 19 step reactions (Homma 2001), are used to simulate CH_4-O_2-N_2 reaction in turbulence. For the three-dimensional case, a reduced kinetic mechanism (MeCH-19) is used.

To investigate the accuracy of the reduced kinetic mechanism, results of two-dimensional DNS with different kinetic mechanisms are compared. It was shown that distributions of important properties such

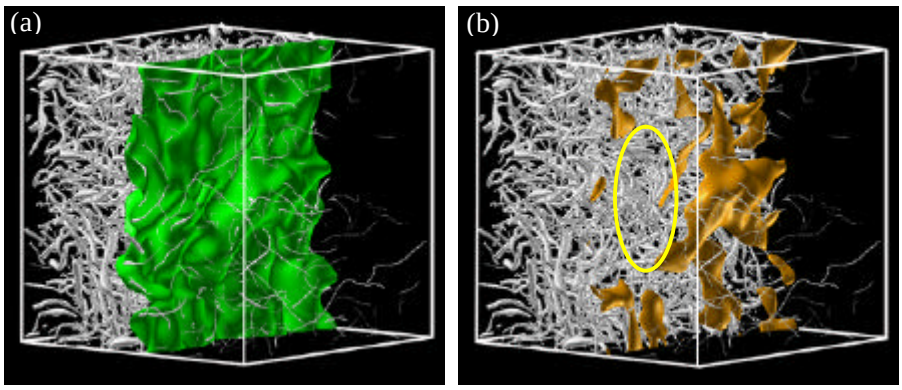

Fig. 14 Contour surfaces of temperature (T=1400K) the heat release rate ($DH>DH_L$) with the axes of the fine scale eddies for methane-air turbulent premixed flames.

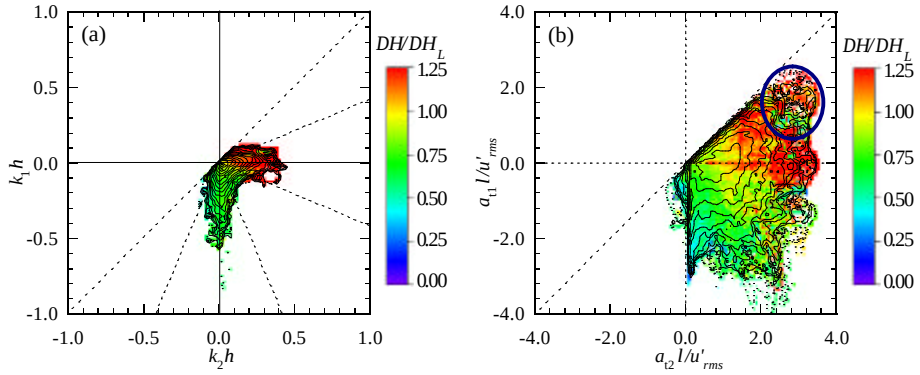

Fig. 15 Mean local heat release rate conditioned with the principal curvatures (a) and mean local heat release rate conditioned with the tangential strain rates (b) for methane-air turbulent premixed flames.

as temperature, major species and heat release rate obtained by the reduced kinetic mechanism (MeCH-19) coincide very well with those obtained by GRI mech. 2.11 except for the minor species which are calculated by assumptions of the steady state. The burning velocity obtained by Miller and Bowman is a little bit high compared with GRI Mech. 2.11 and MeCH-19. This difference is caused by reaction rates related to CH_4 and inherent characteristics of the kinetic mechanism. The use of MeCH-19 reduces computational time and memory to about 1/8 and 1/2, respectively. Since the availability of MeCH-19 is verified by these preliminarily two-dimensional DNS, three-dimensional DNS of methane-air turbulent premixed flames are conduced with MeCH-19. Inflow boundary condition for chemical species is set to be methane-air mixture with f=1.0 at 0.1MPa and 950K. Computational domain is selected to be 5.5mm $\times$5.5mm$\times$5.5mm and 513$\times$192$\times$192 grid points are used. Fully-developed homogeneous isotropic turbulence of which Reynolds number based on Taylor micro scale is about 37.4 is used for initial and inflow boundary condition for the velocity field. The present DNS (u'_{rms}/S_L = 5.80 and l/d_F = 3.28) is classified into the thin reaction zone on the turbulent combustion diagram by Peters (1999).

In Fig. 14, contour surfaces of temperature (T=1400K) and heat release rate (DH/DH_L > 1.0) are shown with axis of the coherent fine scale eddies. Similar to our previous DNS of hydrogen-air turbulent premixed flames, flame fronts are distorted by the fine scale eddies in the unburned turbulence. Compared with hydrogen-air turbulent premixed flames, fluctuation of the heat release rate along to the flame fronts is very large for the present methane-air flame. The maximum heat release rate reaches to 2.0DH_L and minimum one is less than 0.4DH_L. As denoted by a circle in Fig. 14, very large low heat release rate regions are created for methane-air case. The low heat release rate regions correspond to the local extinction of the turbulent premixed flames. Note that local extinction has not been observed for hydrogen-air premixed flames even for the same turbulence intensity (Tanahashi *et al.* 2002). Figure 15 shows mean heat release rate conditioned with the curvatures and the tangential strain rates for the methane-air case. For methane-air turbulent premixed flame, absolute values of the principal curvature are relatively small for the flame elements convex toward the burned side. Furthermore, no clear relation between the curvatures and heat release rate can be observed. However, the local heat release rate shows strong dependence on the tangential strain rates. Similar to the lean hydrogen-air turbulent premixed flames, flame elements under the strong stretching into two tangential directions show high heat release rate. However, flame elements under the excessive strain rates show lower heat release rate as shown in Fig. 15(b). These flame elements exist outer border of the large low heat release rate regions in Fig. 14.

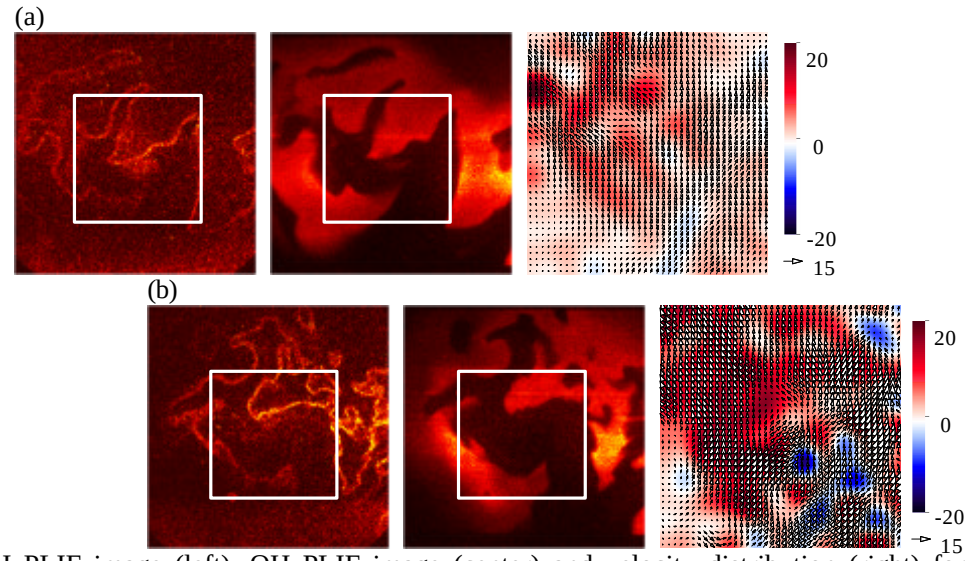

Fig. 16 CH PLIF image (left), OH PLIF image (center) and velocity distribution (right) for different Reynolds number. (a) Re_l=63.1 and (b) Re_l=115.0. Visualized domain size is 31mm×31mm for PLIF images and 16.2mm×16.2mm for velocity field (white box in CH and OH images).

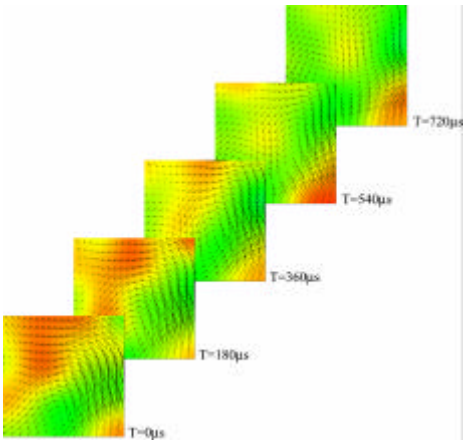

Fig. 17 Time-series vector maps of turbulent swirling flows(11.1kHz).

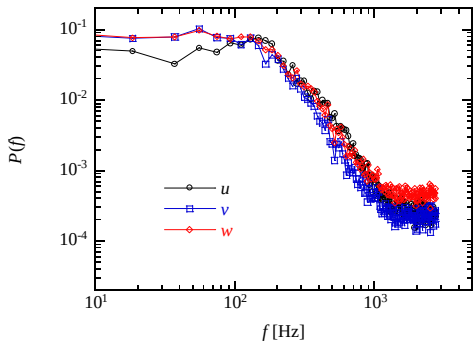

Fig. 18 Power spectrums of the three velocity components obtained by the time-resolved stereoscopic PIV in turbulent swirling flows.

Therefore, the local extinction may relate with appearance these flame elements.

4. Developments of Advanced Experimental Methods for Turbulent Combustion

4.1 Simultaneous CH-OH PLIF Stereoscopic PIV

In addition to DNS, simultaneous CH-OH PLIF and stereoscopic PIV have been developed to investigate local flame structure of turbulent premixed flames (Tanahashi *et al*. 2004b, 2005). In the simultaneous CH-OH PLIF/PIV, high-speed CMOS cameras were adopted to capture the clear stereoscopic particle images without contamination by the flame radiation. The effects of scattering of CH PLIF laser by tracer particles are investigated carefully to improve signal-to-noise ratio in CH fluorescence images. The developed simultaneous two radical concentrations and three component velocity measurement on a two-dimensional plane was applied for relatively high Reynolds number turbulent premixed flames in a swirl-stabilized combustor. All measurements were conducted for methane-air premixed flames in the corrugated flamelets regime. Figure 16 shows results of simultaneous CH and OH PLIF and stereoscopic PIV for different Reynolds number. The Reynolds number dependence of the flame front was clearly captured by the simultaneous CH-OH PLIF and stereoscopic PIV measurement. Simultaneous CH and OH images suggest that the presence of the isolated burned gas in the unburned mixture and the isolated unburned mixture in the burned side which have been predicted by DNS (Nada *et al.* 2004). Strong three-dimensional velocity fluctuation, which is measured by the stereoscopic PIV, implies that misunderstanding of the flame/turbulence interactions would be caused by the analysis of two-component velocity distribution in a cross section. Detailed analysis of simultaneous CH and OH images has been compared with the results of 3D DNS. To investigate statistical characteristics of the flame front, flame front are identified from CH and OH images. Flame front was determined from CH PLIF image and a

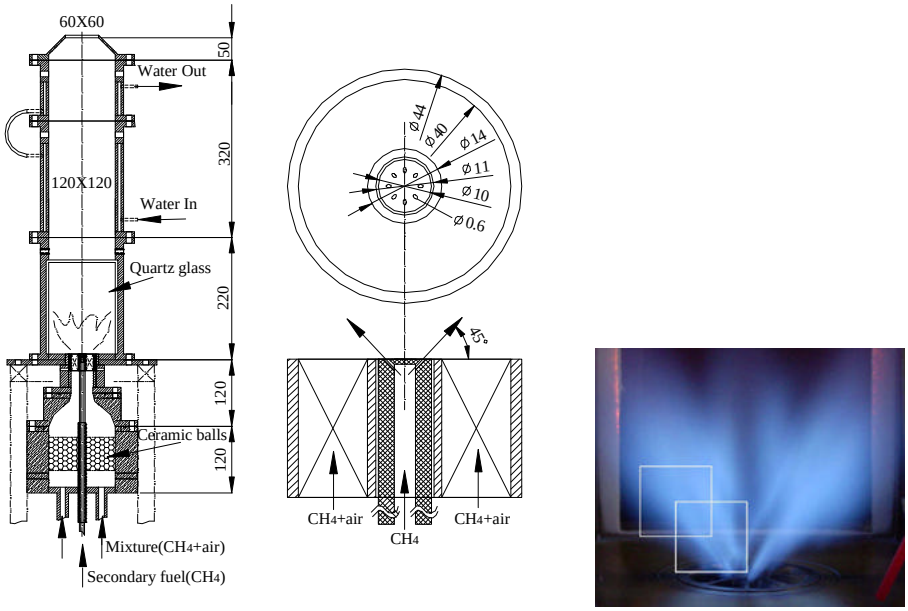

Fig. 19 Swirl-stabilized burner and direct photograph of turbulent premixed flame for f=0.7 and Q=300 l/min.

unit vector normal to the flame front was estimated from the gradients of OH at the flame front. The curvature is ranging in $|k| < 1/h$ and the minimum curvature radius of the flame front is Kolmogorov scale for all Reynolds number and equivalence ratio, which coincides with our previous DNS results (Tanahashi *et al.* 2000, Tanahashi *et al.* 2002, Nada *et al.* 2004). The tangential strain rate on the flame surface was also evaluated from the PIV results. It has been shown that the tangential strain rate is of the order of u'_{rms}/l and shows good agreement with DNS of hydrogen-air and methane-air turbulent premixed flames.

4.2 Time-Resolved Stereoscopic PIV

To investigate velocity fluctuations in combustors, a time-resolved stereoscopic digital PIV system has been developed with high-repetition-rate Nd:YAG lasers for industrial processing and high-speed CMOS cameras (Tanahashi *et al.* 2003, 2004c). The developed system was applied to the velocity measurement of a turbulent jet and a swirl-stabilized combustor. Figure 17 shows time-series vector maps of turbulent swirling flows. This measurement is conducted with 11.1kHz, 256 × 256 pixels and Dt = 30μs for 4.4mm × 4.4mm region. Velocity magnitude across the measurement plane is shaded and shown with velocity vector in the measurement plane. The velocity from behind the sheet to the front has positive value and is denoted by red color. It is shown that velocity measurement up to 26.7kHz is possible and the results represent dynamics of the turbulence structure very well. Accuracy of several PIV algorithms such as a spatial-temporal filter method, a 2-step hierarchical method and a window-offset method have shown for the time-resolved measurement. Figure 18 shows power spectrums of the three velocity components obtained by the time-resolved stereoscopic PIV in turbulent swirling flows. The energy spectrum of out-of-plane velocity component (w) obtained in the present study shows slightly larger values in high frequency region. Although the accuracy of out-of-plane velocity component is a little bit lower than other velocity components, this time-resolved stereoscopic PIV system provides temporal developments of three component velocities in a two-dimensional plane, and gives useful information for understandings the turbulent structures in detail. This system is potentially applicable from several hundred Hz to several tens kHz.

5 Combustion Noise Controls base on Local Flame Structure

5.1 Combustion Controls by Secondary Fuel Injection

Based on fundamental studies described above, controls of a swirl-stabilized combustor have been conducted by using secondary fuel injection (Choi *et al.* 2005). Figure 19 shows the schematics of the swirl-stabilized burner and a direct photograph of methane-air turbulent premixed flame at stoichiometric condition with a flow rate Q=300 l/min. This combustion rig consists of a contraction section, a swirl nozzle section and combustion chamber. The inner diameter of 120mm in the contraction section is reduced to 40mm diameter. The swirl nozzle of 40mm inner diameter was mounted on the contraction section. The inner cross-section of combustion chamber was 120mm × 120mm, and the length of the

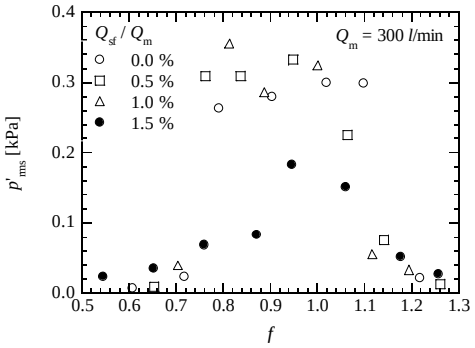

Fig. 20 Pressure fluctuations in the swirl-stabilized combustor with secondary fuel injection.

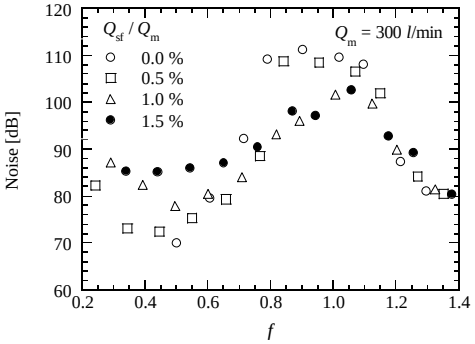

Fig. 21 Combustion noise from in the swirl-stabilized combustor with secondary fuel injection.

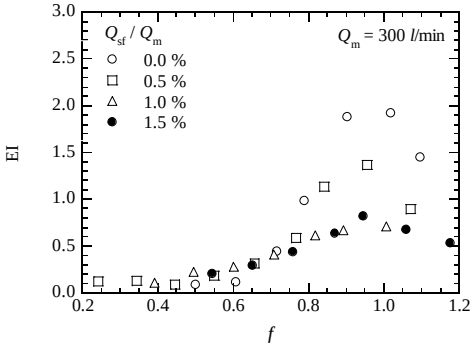

Fig. 22 Emission index of the swirl-stabilized combustor with secondary fuel injection.

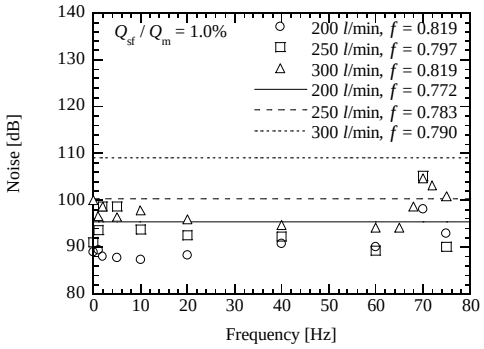

Fig. 23 Effects of injection frequency of the secondary fuel on combustion noise.

chamber was 550mm. On each side of combustion chamber, a silica glass plate of 120mm× 170mm and 5mm thickness was installed to allow optical access. The swirl nozzle has swirl vanes of 14mm inner diameter and 40mm outer diameter, inclined 45 degree from the nozzle axis. Although a secondary fuel nozzle was mounted at center of the swirl vanes, this nozzle was not used in the present study. The premixed methane-air mixture pass through the swirl vanes and the flame was stabilized at swirl vanes as shown in the direct photograph.

Figure 20 shows pressure fluctuations with secondary fuel injection. In this study, Q_m and Q_{sf} denote the mixture flow rate and secondary fuel flow rate, respectively. Regardless of mixture flow rates, the r. m. s. value of pressure fluctuations shows significantly large values between f = 0.8 and 1.1. With increasing mixture flow rate, effect of secondary fuel on pressure fluctuations becomes weak. However, if the secondary fuel injection exceeds 1.5% of mixture flow rate, the r. m. s. of pressure fluctuations decreases drastically. Figure 21 shows noise level for the secondary fuel injection. Although the r. m. s. of pressure fluctuations increased with secondary fuel injection from 0.5% to 1.0% of secondary fuel injection, noise level decreased significantly when the secondary fuel exceeds 1.0% even though there are a little bit increase of noise level at lean conditions. It can be seen that the noise level is decreased about 10dB for f =0.8-1.0. Near f =0.8 for Q_m=300 *l*/min case, large noise level reduction of 20dB is observed for 1.0% secondary fuel injection, whereas the r. m. s. of pressure fluctuation is larger than that without secondary fuel condition.

If the injected pure methane reacts as a diffusion flame, a large amount of nitric oxides will be produced. Figure 22 shows effects of the secondary fuel injection on emission index. For the case without secondary fuel injection, emission index also shows a large value in the region of large oscillation and noise for all flow rates conditions. This large amount of emission index is ascribed to the combustion oscillating with complicated flame structures. With the injection of secondary fuel, it is observed that the emission index decreases in the large pressure fluctuating region. However, effect of secondary fuel injection on lean and rich conditions is small. In addition, the lean blowout limits are extended to quite lean condition by injecting secondary fuel. From the above result, it can be seen that secondary fuel injection is effective to suppress combustion oscillation, to prevent lean blowout and to reduce emission index.

Figure 23 shows the effect of injection frequency of secondary fuel on combustion noise. For comparisons, results without secondary fuel injection are also plotted. By conducting frequency controls of the secondary fuel injection, noise level decreases and maximum noise reduction is achieved at about 40Hz for Q =300 *l*/min. There is a most relevant frequency for the noise reduction for each combustion

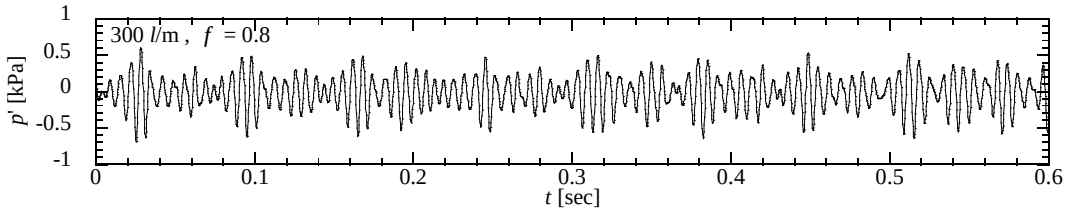

Fig. 24 Time-series signal of pressure fluctuations in the combustor.

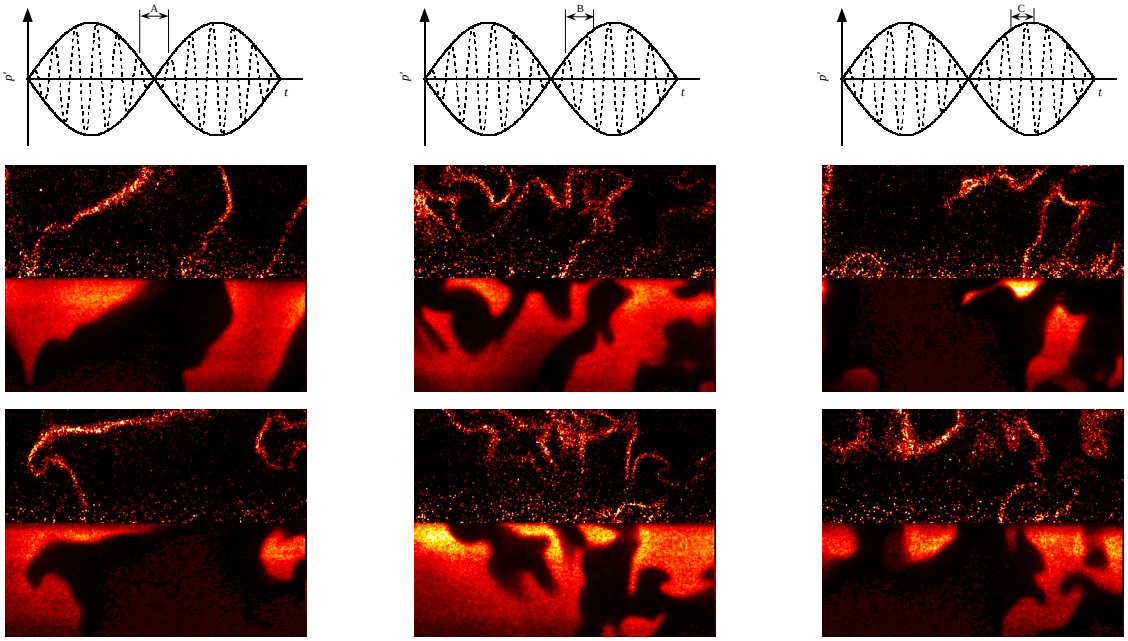

(a) A region (b) B region (c) C region

Fig. 25 CH fluorescence images (upper) and OH fluorescence images (lower) conditioned with pressure fluctuations in the combustor (Q=300[l/min], f=0.8).

condition. Peak frequency of the pressure fluctuations in the combustor is in the range of 117-130Hz, which coincides with the natural acoustic mode of the combustor. Since the most relevant frequency of the secondary fuel injection is far from the natural acoustic mode, this control does not correspond to addition of an energy source out of phase with pressure fluctuation in the combustor. The reason of this noise reduction can be explained from the local flame structure.

Figure 24 shows the time-series signal of pressure fluctuations at 300 [l/min] and f=0.8. Since pressure fluctuations in the combustor have several peaks in the frequency domain, actual pressure signals have beat frequency. This beat frequency is about 30-40Hz. To investigate the relation between beat frequency and local flame structure, we classified into three large groups, that is, small pressure fluctuating region (A), middle pressure fluctuating region (B) and large pressure fluctuating region (C) in the long period of pressure fluctuations, as shown schematically in Fig. 25. Figure 25 shows CH/OH PLIF images in the flame zone for each pressure condition. For the small pressure fluctuating region (A), the flame front is very smooth and formation of flame cusps is also rare compared to other conditions. For the middle pressure fluctuating region (B), the degree of flame wrinkling increases compared to A region. The flame is much more wrinkled and many small-scale flame cusps were observed. For the large pressure fluctuating region (C), we can observe that small-scale flame cusps remained though flame front became rare compared to B region. These results show that local flame structure well reflects the beating frequency. The 40Hz secondary fuel injection breaks down this coupling between the local flame structure and pressure fluctuation.

5.2 Local Flame Structure in Noise-Controlled, Swirl-Stabilized Combustor

To investigate mechanism of the combustion noise reduction by the secondary fuel injection, CH-OH PLIF measurements have been conducted in two important region of the combustor. In Fig. 19, measurement regions are denoted by white boxes. First one is re-circulation zone near the secondary fuel injection nozzle and second one is in the flame zone. In Figs. 26 and 27, OH distributions obtained in the re-circulation zone are shown for no secondary injection and 1%-contineous secondary fuel injection cases. In the case of no secondary fuel injection, OH has large fluctuation in space and time. However, for 1%-contineous secondary fuel injection case, spatial and temporal fluctuation in OH is reduced.

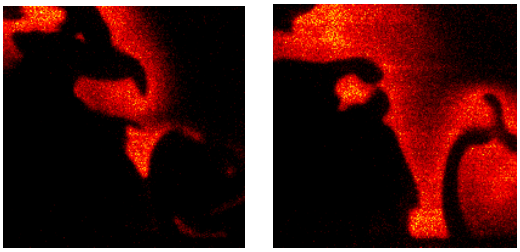

Fig. 26 OH PLIF results in the re-circulation zone for no secondary fuel injection.

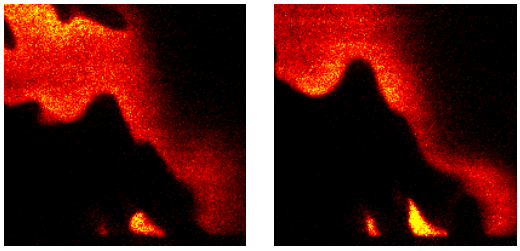

Fig. 27 OH PLIF results in the re-circulation zone for 1%-contineous secondary fuel injection.

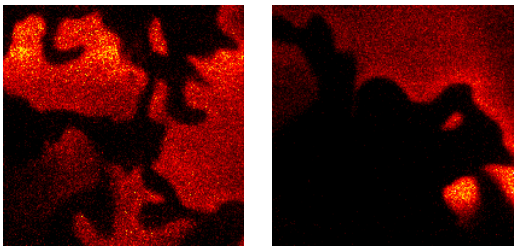

Fig. 28 OH PLIF results in the flame zone for no secondary fuel injection (a) and for 1%-contineous secondary fuel injection (b).

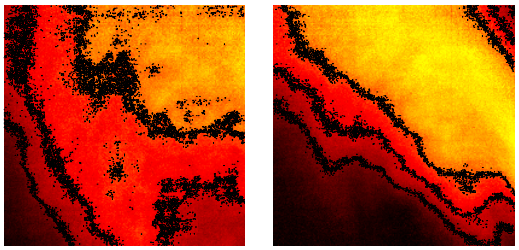

Fig. 29 Probability of existence of flame front for no secondary fuel injection (a) and for 1%-contineous secondary fuel injection (b).

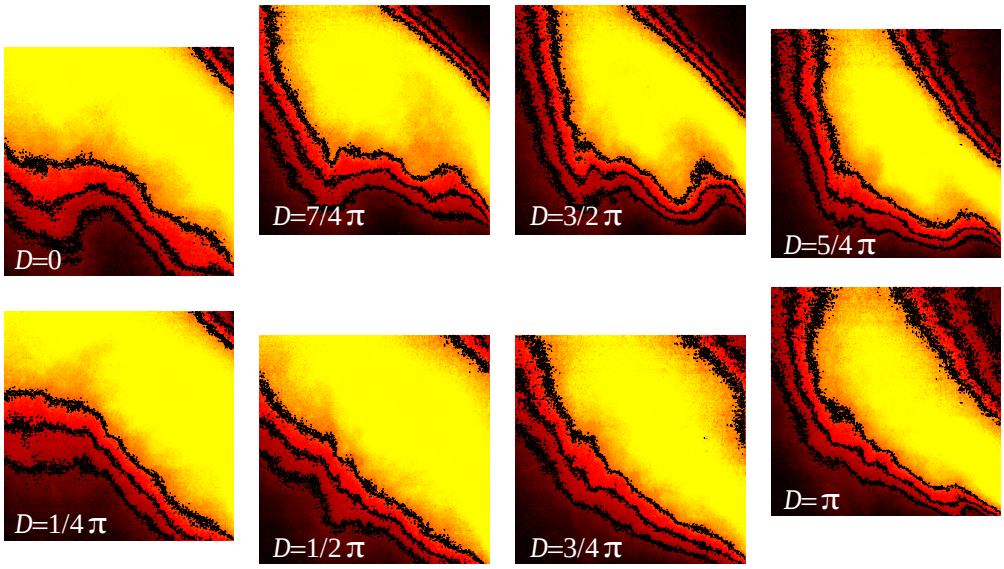

Fig. 30 Probability of existence of flame front for 1%-40Hz secondary fuel injection. Probabilities are phase-locked with control signal for the secondary fuel injector.

Characteristics of OH distributions in this region do not depend on the frequency of secondary fuel injections. Since CH PLIF signals in this region is quite low for all cases, the secondary fuel dons not burn like a diffusion flame, which is reason of low emission index shown in Fig. 22. Therefore, the secondary fuel injection reduces the spatial and temporal fluctuation of the high temperature fluid in the re-circulation zone independent on the frequency of the injection.

In Fig. 28, OH distribution in the flame zone is shown for no secondary injection and 1%-contineous secondary fuel injection cases. OH radicals for no secondary injection show very complicated distribution, whereas those for 1%-contineous secondary fuel injection have relatively low fluctuation. In this study, probability of existence of the flame front is evaluated from OH PLIF results as shown in Fig. 29. In Fig. 29, probability of flame front existence is denoted by color. Black means zero probability and unburned gas always exist, and yellow also means zero probability and burned gas always exist. The region with red represents active flame zone. Solid lines in Fig. 29 represent 30% flame existence in the unburned side, 50% and 30 % flame existence in the burned side, respectively. Figure 29 suggests that the secondary fuel change local flame structure in the flame zones. Without the secondary fuel injection, flame fronts have large spatial and temporal fluctuation (flame bush is very wide). However, by adding continuous fuel injection, flame fronts are located in the relatively narrow region (flame bush become thin). Figure 30 shows similar probability for 1% 40Hz secondary fuel injection. Probability is evaluated for

each phase of the secondary fuel injection by conducting PLIF which are phase-locked with the control signal to the secondary fuel injector. As for the cases of the frequency control of the injection, the width of the flame bush becomes thinner and is confined to tiny space at the most relevant frequency. These characteristics of the re-circulation zone and the flame bush correspond to controls of the sound sources which have been shown by DNS in Sec. 2. These results suggest that turbulent combustion controls base on the local flame structure is possible by frequency control of the secondary fuel injection.

6. Summary

In this paper, studies on turbulent combustion controls conducted, which are supported by the 'Smart Control of Turbulence' project in last 5 years, have been summarized. The results of our study suggest that turbulent combustion controls based on the local flame structure will be available to construct high efficiency and low emission combustor. In this study, diode laser absorption sensor has been developed to realize active control of the turbulent combustion. However, those results are shown in another paper by combustion group in this project (Zimmer *et al.* 2005).

References

Baum, M., Poinsot, T. J., Haworth, D. C. and Darabiha, N., (1994), *J. Fluid Mech.*, 281:1-32.

Bell, J. B., Day, M. S. and Grcar, J. F., (2002), *Proc. Combust. Inst.*, 29:1987-1993.

Blonbou, R., Laverdant, A., Zaleski, S., and Kuentzmann, P., (2000), *Proc. Combust. Inst.*, 28:747-755.

Borghi, R. W., (1985), *Recent Advances in Aeronautical Science*, Plenum, p. 117.

Broda, J. C, Seo, S., Santoro, R. J., Shirhattikar, G., and Yang, V., (1998), *Proc. Combust. Inst.*, 27:1849-1856.

Candel, S. and Poinsot, T., (1990), *Combust. Sci. Tech.*, 70:1-15.

Chen, J. H., Echekki, T. and Kollmann, W., (1998), *Combust. Flame*, 116:15-48.

Choi, G.-M., Li, Y., Tanahashi, M. and Miyauchi, T., (2003), *Turbulence and Shear Flow Phenomena -3*, Vol. 2, pp.279-284.

Choi, G.-M., Tanahashi, M. and Miyauchi, T., (2005), *Proc. Combust. Inst.*, 30:1807-1814.

Colonius, T., Lele, S. K. and Moin, P., (1994), *J. Fluid Mech.*, 260: 271-298

Colonius, T., Lele, S. K. and Moin, P., (1997), *J. Fluid Mech.*, 330: 375-409

Delabroy, O., Haile, E., Lacas, F., Candel, S., Pollard, A., Sobiesiak, A., Becker, H. A., (1998), *Exp. Thermal Fluid Sci.*, 16:64-75.

Di Benedetto, A., Marra, F. S., and Russo, G., (2002), *Sci. and Tech.*, 174(10):1-18.

Echekki, T. and Chen, J. H., (1996), *Combust. Flame*, 106:184-202.

Gulati, A., and Mani, R., (1992), *J. Prop. Power* 8(5):1109-1115.

Gutheil, E., Balakrishnan, G. and Williams, F. A., (1993), *Reduced Kinetic Mechanisms for Applications in Combustion Systems*, Springer-Verlag, p. 177.

Harper, J., Johnson, C. J., Neumeier, Y., Lieuwen, T., and Zinn, B. T., *AIAA Paper* #2001-0486.

Homma, R., (2001), *Proc. 29th Jpn. Symp. Combust.*, pp.533- 534

Hong, B-S., Ray, A., and Yang, V., (2002), *Combust. Flame*, 128:242-258.

Jenkins, K. W. and Cant, R. S., (2002), *Proc. Combust. Inst.*, 29:2023-2029.

Lee, J. G., Kim, K., and Santavicca, D., (2000), *Proc. Combust. Inst.*, 28:739-746.

Li, Y., Tanahashi, M. and Miyauchi, T., (2000a), *Trans. JSME*, 66(646):1527-1534.

Li, Y., Tanahashi, M. and Miyauchi, T., (2000b), *Trans. JSME*, 66(648): 2117-2124.

Li, Y., Tanahashi, M. and Miyauchi, T., (2001), *JSME Int. Journal*, Series B, 44(4):505-512.

Lieuwen, T., and Zinn, B. T., (2000), *AIAA paper*, 2000-0707.

Lighthill, M. J., (1952), *Proc. R. Soc. Lond.*, A 211: 564-587

Lilley, G. M., (1994), *Theoret. Comput. Fluid Dynamics*, 6: 281-301.

Miller, J. A. and Bowman, C. T., (1989), *Prog. Energy Combust. Sci.*, 15:287-338.

Mitchell, B. E, Lele, S. K. and Moin, P., (1995), *J. Fluid Mech.*, 285: 181-202.

Miyauchi, T., Tanahashi, M. and Li, Y., (2001), *Smart Control of Turbulent Combustion*, pp.28-38.

Murugappan, S., Gutmark, E. J., Acharya, S., and Kristic, M., (2000), *Proc. Combust. Inst.*, 28:731-737.

Nada, Y., Tanahashi, M. and Miyauchi, T., (2004), *J. Turbulence*, 5:16.

Paschereit, C. O., Gutmark, E., and Weisenstain, W., (1999), *Physics Fluids*, 11(9):2667-2678.

Peters, N., (1986), *Proc. Combust. Inst.*, 21:1231-1250.

Peters, N., (1992), *J. Fluid Mech.*, 384:107-132.

Poinsot, T., Le Chatelier, C., Candel, S. M., and Esposito, E., (1986), *J. Sound Vibr.*, 107(2):265-278.

Poinsot, T., Veynante, D. and Candel, S., (1990), *Proc. Combust. Inst.*, 23:613-619.

Poppe, C., Sivaegaram, S., and Whitelaw, J. H., (1998), *Combust. Flame*, 113:13-26.

Powell, A., (1964), *J. Acoust. Soc. Am.*, 36: 177-195

Rayleigh, L. *Theory of Sound*, Dover, New York, 1945.
Saito, T., Tanahashi, M. and Miyauchi, T., (2002), J. *Combust. Society of Japan*, 44:243-252.
Samaniego, J. M., Yip, B., Poinsot, T., and Candel, S., (1993), *Combust. Flame*, 94:363-380.
Sivasegaram, S., Tsai, R. F., and Whitelaw, J. H., (1995), *Combust. Sci. Technol.* 10(5):67-83.
Sreedhara, S. and Lakshmisha, K. N., (2002), *Proc. Combust. Inst.*, 29:2051-2059.
Tanahashi, M., Miyauchi, T., Nada, Y. and Imamura, Y., (1998), *Trans. JSME*, 64:2662-2668.
Tanahashi, M., Fujimura, M. and Miyauchi, T., (2000a), *Proc. Combust. Inst.*, 28:529-535.
Tanahashi, M., Iwase, S., Uddin, A., Takata, N. and Miyauchi, T., (2000b), *Therm. Sci. Eng.*, 8:29-38.
Tanahashi, M., Iwase, S. and Miyauchi, T., (2001), *J. Turbulence*, 2: 006.
Tanahashi, M., Nada, Y., Ito, Y. and Miyauchi, T., *Proc. Combust. Inst.*, (2002) 29:2041-2049.
Tanahashi, M., Fukuchi, Y., Choi, G.-M., Fukuzato, K. and Miyauchi, T., (2003), *Turbulence, Heat and Mass Transfer 4*, pp.245-252.
Tanahashi, M., Kang, S.-J., Miyamoto, T., Shiokawa, S.,and Miyauchi, T., (2004a), *Int. J. Heat and Fluid Flow*, 25:331-340.
Tanahashi, M., Choi, G.-M., Murakami, S., Fukuchi Y. and Miyauchi, T., (2004b), *Proc. 12th Intl. Symposium on Appl. of Laser Techniques to Fluid Mechanics*, CD-ROM.
Tanahashi, M., Fukuchi, Y., Choi, G.-M., Fukuzato, K. and Miyauchi, T., (2004c), *Proc. 12th Intl. Symposium on Appl. of Laser Techniques to Fluid Mechanics*, CD-ROM.
Tanahashi, M., Kikuta S. and Miyauchi, T., (2004d), *57th Annual Meeting of the Division of Fluid Dynamics*, American Physics Society.
Tanahashi, M., Murakami, S., Choi, G.-M., Fukuchi, Y. and Miyauchi, T., (2005), *Proc. Combust. Inst.*, 30:1665-1672.
Zimmer, L., Tachibana, S., Tanahashi, M., Shimura, M. and Miyauchi, T., (2005), *Proc. 6th Symp. Smart Control of Turbulence*.